

# MITO: Enabling Non-Line-of-Sight Perception using Millimeter-waves through Real-World Datasets and Simulation Tools

Laura Dodds<sup>1,\*</sup>, Tara Boroushaki<sup>1,\*</sup>, Fadel Adib<sup>1,2</sup>  
 {ldodds, tarab, fadel}@mit.edu

<sup>1</sup> Massachusetts Institute of Technology, <sup>2</sup> Cartesian Systems, \* These authors contributed equally

## Abstract

We present MITO, the first dataset of multi-spectral millimeter-wave (mmWave) images of everyday objects. Unlike visible light, mmWave signals can image through everyday occlusions (e.g., cardboard boxes, fabric, plastic). However, due to the dearth of publicly-available mmWave images and the interdisciplinary challenges in collecting and processing mmWave signals, it remains difficult today for computer vision researchers to develop mmWave-based non-line-of-sight perception algorithms and models.

To overcome these challenges, we introduce a real-world dataset and open-source simulation tool for mmWave imaging. The dataset is acquired using a UR5 robotic arm with two mmWave radars operating at different frequencies and an RGB-D camera. Through a radar signal processing pipeline, we capture and create over 580 real-world 3D mmWave images taken from over 76 different objects in the YCB dataset, a standard benchmarking dataset for robotics manipulation. For each object, we provide real-world mmWave images in line-of-sight and non-line-of-sight, as well as RGB-D images and ground truth segmentation masks. We also develop an open-source simulation tool that can be used to generate synthetic mmWave images for any 3D triangle mesh, which achieves a median F-Score of 94% when compared to real-world mmWave images.

We demonstrate the usefulness of this dataset and simulation tool in multiple computer vision tasks in non-line-of-sight. First, we perform object segmentation for mmWave images leveraging the segment anything model (SAM), and achieve a median precision and recall of 92.6% and 64%. Second, we train a classifier that can recognize objects in non-line-of-sight. It is trained on synthetic images and can classify in real-world scenarios with 85% accuracy.

The dataset of images, raw data, and the simulation – along with python and cuda scripts for downloading the dataset, processing the raw data, and visualizing the images – is all available open-source. We believe that MITO will serve as an instrumental resource that enables computer vision researchers to develop algorithms and models for non-line-of-sight perception using mmWaves, and hope that this first-of-its-kind dataset will have a similar impact as early camera-based datasets that paved the way for significant innovations in the field.

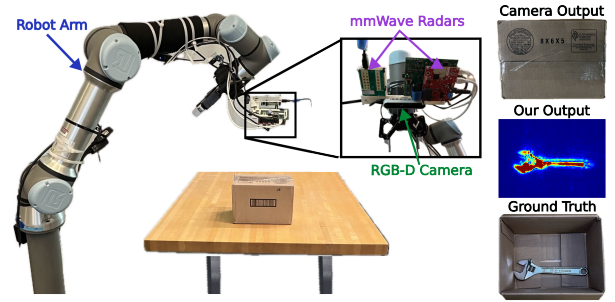


Figure 1. MITO. We use a robotic arm to move mmWave radars throughout the environment. While an RGB-D camera’s output cannot see inside the box, we produce high-resolution non-line-of-sight mmWave images.

## 1. Introduction

Recent decades have witnessed many impressive advancements in computer vision, with state-of-the-art systems capable of high-accuracy object detection, segmentation, classification, and more. One of the main applications of these advances is in robotic manipulation and perception, where autonomous robots are expected to find and retrieve objects and navigate through complex environments spanning warehouses, manufacturing plants, and smart homes.

However, relying primarily on optical perception (e.g., cameras, LiDARs, etc) inherently limits existing systems to line-of-sight.<sup>1</sup> For example, a camera-based system cannot see inside a closed box to confirm e-commerce orders are correct or detect broken objects during shipping. Nor is it feasible for camera-based robots to efficiently plan complex, multi-step tasks in practical environments where required objects may be fully occluded.

Instead, it is possible to produce non-line-of-sight (NLOS) images using millimeter-wave (mmWave) radars[9]. Unlike visible light, mmWave wireless signals can traverse everyday occlusions such as cardboard, fabric, and plastic. This allows mmWave radars to image objects in non-line-of-sight, similar to how airport security scanners produce high-resolution NLOS images of passengers to detect hidden weapons. With the emergence of low-cost mmWave radars, it is possible to build pervasive autonomous systems with this NLOS imaging capability. For example, using mmWave radars attached to a robotic arm (Fig. 1), we can produce a NLOS mmWave image of a

<sup>1</sup>While some visible-light systems can rely on reflected laser light to image objects around the corner, they cannot image fully occluded items (e.g., within a closed box).

wrench within a closed box.

However, to achieve the many possible applications of NLOS imaging, we need to be able to *perceive* (e.g., segment, classify, etc) objects within these images. Unfortunately, these images are fundamentally different from visible-light images in multiple ways. First, they suffer from radar-specific artifacts; for example, the much longer wavelength of millimeter-waves versus visible light (hundreds of nanometers) results in fundamentally different specular and diffuse properties of imaged objects. Second, mmWave images have no color information. Third, they are complex-valued.<sup>2</sup> Therefore, since the majority of existing perception algorithms have not been trained on these mmWave images, they need to be adapted for NLOS perception; in some cases, we may require entirely new algorithms or models to enable mmWave-based perception to approach the accuracy of visual-light-based perception (as we show in this paper).

Inspired by how early imaging datasets, such as MSRC[21], Pascal[20], Berkeley 3D[27], and YCB[17], paved the way for many advancements within computer vision, we believe that a dataset of mmWave images of everyday objects is fundamental for enabling pervasive NLOS perception.

In this paper, we present MITO.<sup>3</sup> To the best of our knowledge, this is the first dataset of multi-spectral mmWave images for everyday objects. It builds on the YCB dataset, a standard dataset for robotic manipulation which already provides 2D and 3D camera scans of many common objects. In building MITO, we introduce a few key contributions:

- **Real World Dataset.** Using a custom-built robotic imaging system and signal processing pipeline, we capture images of 76 objects in the YCB dataset (out of a total of 80 objects). We captured over 580 real-world images of objects in both line-of-sight and non-line-of-sight. For each object, we capture mmWave images at multiple different frequencies. The frequency of the signal introduces an important tradeoff between the image resolution and the ability for the radars to image objects under thick occlusions. We also include the RGB-D images of the objects (when in LOS) and a ground truth object segmentation produced with the segment-anything model.
- **Open-Source mmWave Simulation Tool.** We also created an open-source simulation tool that can produce synthetic mmWave images for any 3D triangle mesh. Given the million of meshes available online[1, 10], this provides the flexibility to produce a significant synthetic dataset. Importantly, different materials interact differently with mmWave signals and therefore produce differ-

<sup>2</sup>Interestingly, the values are dependent on not only the location of the object, but also the material and texture.

<sup>3</sup>mmWave Imaging Through Occlusions

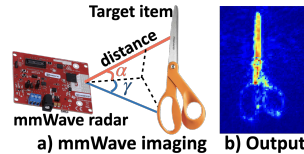


Figure 2. **mmWave Imaging** a) mmWave radars estimate range and angle-of-arrival to produce b) reflection maps.

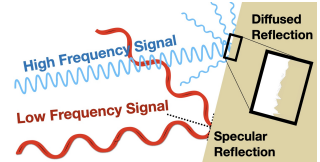


Figure 3. **Diffuse and Specular Reflections.** The frequency of a signal changes the type of reflections it experiences for the same surface.

ent images. Therefore, we build two different modeling methods into our simulation, the combination of which can be used to simulate a wide range of material properties. When compared to real-world mmWave images, our simulation achieves a median 3D F-Score of 94%.

- **Example Computer Vision Tasks.** Using MITO, we demonstrated two potential computer vision tasks in non-line-of-sight. First, we show object segmentation, using the segment-anything model (SAM)[28] and a mmWave power-based prompter. Second, we show object classification, which is trained entirely on synthetic images and is able to classify objects in real-world images with 85% accuracy.

The dataset, all code, and a video is available here:

[https://github.com/signalkinetics/MITO\\_Codebase](https://github.com/signalkinetics/MITO_Codebase)

## 2. Background

### 2.1. mmWave Imaging

In this section, we describe how mmWave imaging works at a high level, and refer readers to [35] for more details. A mmWave radar transmits wireless signals with millimeter-wave wavelengths, captures their reflections, and uses them to generate 3D images, as shown in Fig. 2a. It uses two core signal processing techniques. First, it estimates distance using chirp signals. Specifically, by comparing the frequency between the transmitted and received signals it can estimate the distance of each reflection. Second, it measures the angle of a reflection (in both azimuth and elevation) by comparing the received signals between different antennas. By measuring the reflection power emanating from each voxel in 3D space (defined by distance, elevation angle, and azimuth angle), it can perform 3D reconstruction.

The captured image can be represented as a heatmap as shown in Fig. 2b, where red represents high intensity reflection and blue represents low intensity. It is important to note that this visualization is a 2D projection of the 3D image. Mathematically, since every sample from the radar is a complex number with a phase and an amplitude, we can combine them with the following equation:

$$I(x, y, z) = \sum_{k=1}^K \sum_{j=1}^N S_{j,k} e^{\frac{j2\pi d(x,y,z,k)}{\lambda_j}} \quad (1)$$

where  $I(x, y, z)$  is the complex mmWave image at location  $(x, y, z)$ ,  $K$  is the number of antennas,  $N$  is the number of samples in each chirp,  $S_{j,k}$  is the  $j^{\text{th}}$  sample of the chirp

from the  $k^{\text{th}}$  antenna, and  $\lambda_j$  is the wavelength of the signal at sample  $j$ , which is proportional to the speed of light  $c$  and the frequency  $f$  as  $\lambda = \frac{c}{f}$ .  $d(x, y, z, k)$  is the round-trip distance from the  $k^{\text{th}}$  antenna (at location  $p_k$ ) to the point  $(x, y, z)$  and is defined as  $d(x, y, z, k) = 2\|(x, y, z) - p_k\|$ .

### 2.1.1 Resolution.

One important characteristic of a mmWave image is its resolution. The resolution in range (depth) is determined by the *bandwidth*, or the range of frequencies that the chirp covers. We compute the depth resolution  $\delta_z$  as:

$$\delta_z = \frac{c}{2B} \quad (2)$$

where  $c$  is the speed of light, and  $B$  is the bandwidth of the signal. The resolution in the horizontal and vertical dimensions is dependent on the *aperture*, or the distance between the first and last antenna in that dimension.

$$\delta_x = \frac{\lambda z_0}{2D_x} \quad \delta_y = \frac{\lambda z_0}{2D_y} \quad (3)$$

where  $\delta_x$  and  $\delta_y$  are the resolution in the  $x$  and  $y$  dimensions, respectively.  $z_0$  is the range to the target, and  $D_x$  and  $D_y$  are the apertures in  $x$  and  $y$  dimensions, respectively.

### 2.1.2 Synthetic Aperture Radar (SAR) Imaging.

As described above, it is desirable to increase the aperture to increase the image resolution (Eq. 3). Instead of creating a large aperture through a large number of physical antennas on the radar, it is possible to perform SAR imaging. In this method, one set of transmitters/receivers are moved through the environment, taking measurements from different locations, and constructing a “synthetic aperture”. These measurements can be combined through Eq. 1 to provide the same resolution as a physical aperture.

## 2.2. Impact of Frequency.

One important question is what frequency to use for imaging. The frequency introduces an important tradeoff. First, higher frequencies result in higher resolution (as seen in Eq. 3). On the other hand, higher frequency signals experience more attenuation, or power loss, as they travel through materials[8]. This means that high frequency signals may not be able to image through as thick of occlusions compared to lower frequencies. This is why MITO’s dataset and simulation tool include multi-spectral mmWave images (i.e., at different frequencies).

## 2.3. Types of Reflections.

mmWave signals primarily exhibit specular (mirror-like) reflections[33]. This characteristic is illustrated in Fig. 3. Due to the significantly longer wavelengths of mmWave signals compared to visible light (millimeters vs nanometers), surfaces that appear diffuse (i.e., omnidirectional) for visible light (blue) often appear specular for mmWave signals (red).

In addition to specular reflections, mmWaves also exhibit strong reflections when a wave strikes a sharp edge of an object, scattering it in multiple directions. This type

of reflection, known as edge diffraction, can impact signal propagation and perception differently from diffuse or specular reflections.

These reflection properties are one fundamental difference between mmWave signals and visible light that necessitates algorithms and models specifically designed for mmWave images.

## 3. MITO: Properties and Structure

In this section, we describe the contents of MITO.

**Objects.** MITO builds on the YCB dataset[17], a standard dataset of objects used for robotic manipulation. The YCB dataset already provides 2D images and 3D scans of 80 everyday objects that we use to simulate synthetic mmWave images of the objects. We have included 76 of these objects in MITO<sup>4</sup>.

**Object Diversity.** Since our dataset represents the vast majority of the YCB dataset, our objects are diverse across shape, size, material, and type. In terms of shape, our dataset includes spherical, flat, curved, and complex shapes. In terms of size, it includes objects whose dimensions range from 1.5cm to 47cm. Our objects include various materials such as wood, plastic (e.g., HDPE, PETE, Polypropylene, Nylon, etc), metal, cardboard, rubber, as well as objects with multiple materials. Additionally, our objects represent a wide range of categories, including household tools (wrench, screwdriver, hammer), groceries (sugar box, soup can, cracker box), kitchen supplies (spatula, plate, skillet), toys (marbles, rubik’s cube, baseball), and office supplies (scissors, dry erase markers).

**Real-World Multi-Spectral mmWave Images.** We provide over 580 3D, complex-valued mmWave images in both line-of-sight (LOS) and non-line-of-sight (NLOS) settings, and at two different frequencies (24GHz and 77GHz).

Recall from Sec. 2.2 that the frequency of the mmWave signal impacts both the resolution of the resulting image and the ability for the signal to traverse through occlusions. For example, we show four example images in Fig. 4. Fig. 4a-b show a 77GHz and 24GHz image of a padlock in LOS, respectively. The 77GHz image is higher resolution, as expected. On the other hand, Fig. 4c-d show 77GHz and 24GHz images of the same object in NLOS (placed underneath cardboard). In this case, the 24GHz image is very similar to the LOS case, while the 77GHz shows some artifacts that were not present in the LOS case. This is because the 24GHz image travels through the cardboard relatively unaffected, while the 77GHz is partially reflected and absorbed by the cardboard. It is our hope that by including two different frequencies, future algorithms can leverage both images to benefit from both high-resolution and robustness to thick occlusions.

**Raw mmWave Data.** In addition to the processed mm-

<sup>4</sup>The remaining 4 items were discarded mainly because we could not obtain the exact items from the YCB dataset to image them.

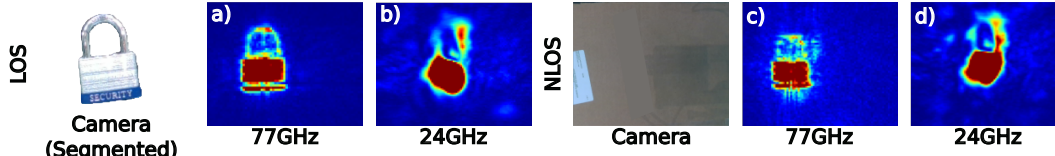


Figure 4. **Multi-Spectral Imaging.** a-b) show 77GHz & 24GHz images for a padlock in LOS. c-d) show the images in NLOS.

Wave images, we also include the raw signals collected during each experiment, as well as the radar’s location for each measurement. The code for processing raw measurements into a mmWave image is included as well. This allows researchers to investigate many different avenues, such as experimenting with other imaging algorithms or evaluating the impact of removing measurements from an experiment.

**RGB-D Images.** For each mmWave image, we also take a corresponding RGB-D image of the object. In the case of a NLOS image, we take the camera image before occluding the object. We also provide the ground truth segmentation mask using the RGB-D images. The camera’s location is also recorded, which allows us to transform the segmentation masks to the same frame as the mmWave images. These transformed masks are also included and can be used to evaluate segmentation and object completion networks.

**Synthetic mmWave Images.** In addition to all the real-world data described above, we also provide a simulation tool to generate synthetic mmWave images, which can be used to increase the volume of data to aid in model training. We include at least 2 different simulation images for each object, along with the simulation tool for producing additional images (See Sec. 5 for more details).

## 4. Data Collection and Validation

Next, we describe how we collect the data in MITO.

### 4.1. Real-World Data Collection

**Object Placement.** Similar to how initial RGB datasets provided images of objects with white backgrounds, our goal in the initial images of MITO is to create a simple image of just the object without a complex background. To do so, we image the objects in two setups, each of which minimizes background reflections in a different way. In the first, we place each object on a tripod<sup>5</sup> such that there is no surface directly below the object, preventing any strong reflections from the background. In the second, we place the object directly on a styrofoam block, since styrofoam is largely transparent to mmWave signals[11].

**Data Collection Setup.** We build a robotic system capable of mmWave imaging. We connect a 77GHz radar (TI IWR1443Boost, <\$300[9] and DCA1000EVM, <\$600[2]) and a 24GHz radar (Infineon Position2Go, <\$300[7]), and Intel Realsense D415[26] to an end-effector of a UR5e robotic arm[46] using custom-designed 3D printed parts. At the start of an experiment, the robot moves the camera to the middle of the workspace to take an RGB-D image. Then,

<sup>5</sup>We hot-glue a 3D printed nut to each object, and screw it onto a threaded tripod.

it moves the radars throughout the workspace, covering a rectangular space. The aperture of our experiments range from 55cm by 22cm to 55cm by 29cm.<sup>6</sup> The radars continuously measure mmWave signals while the robot is moving, and the robot records its trajectory over time. After we complete an experiment in LOS, we run an experiment in NLOS without moving the object. We place a layer of cardboard over the object to simulate the case where the object was placed inside a box.

**Robot - Radar Synchronization.** To process the mmWave image, we need to know the location that each measurement was taken (per Eq. 1). To do this, we interpolate the timestamped robot locations to match the timestamp of the radar measurements. Since the robot and radars are controlled from different computers, we set both computers to the same NTP time server to ensure accurate time synchronization.

**mmWave Image Processing.** Next, the raw measurements are processed into a 3D mmWave image by applying Eq. 1. Example images can be seen in Fig. 5, which shows the segmented RGB images (1st column), 77GHz LOS (2nd column), 77GHz NLOS (3rd column), 24GHz LOS (4th column), and 24GHz NLOS (5th column) mmWave images. Additional images are provided in the supplementary.

**Background Measurements.** We also include experiments when the tripod/styrofoam is placed in the scene without any object. This can be used to remove the impact of the tripod/styrofoam from images by subtracting the empty image from the main image[13].

**Ground Truth Segmentations.** Given the RGB-D images of the objects in LOS, we produce ground-truth segmentation masks of the objects in each experiment using the segment-anything model (SAM). We use an interactive interface for SAM to select the points on the RGB picture to use as a prompt for the model. The human annotator continues selecting points until the mask covers the full object. We then align the RGB ground-truth mask with the mmWave image. The details for this alignment can be found in the supplementary material.

## 5. Simulating mmWave Images

In this section, we describe our open-source simulation tool which can be used to generate synthetic mmWave images, and evaluate the simulator’s accuracy.

### 5.1. Simulation Tool

Our simulation tool takes as input a 3D triangle mesh for the target object. These mesh files can be found in ob-

<sup>6</sup>Each experiment uses an aperture which covers the full object.

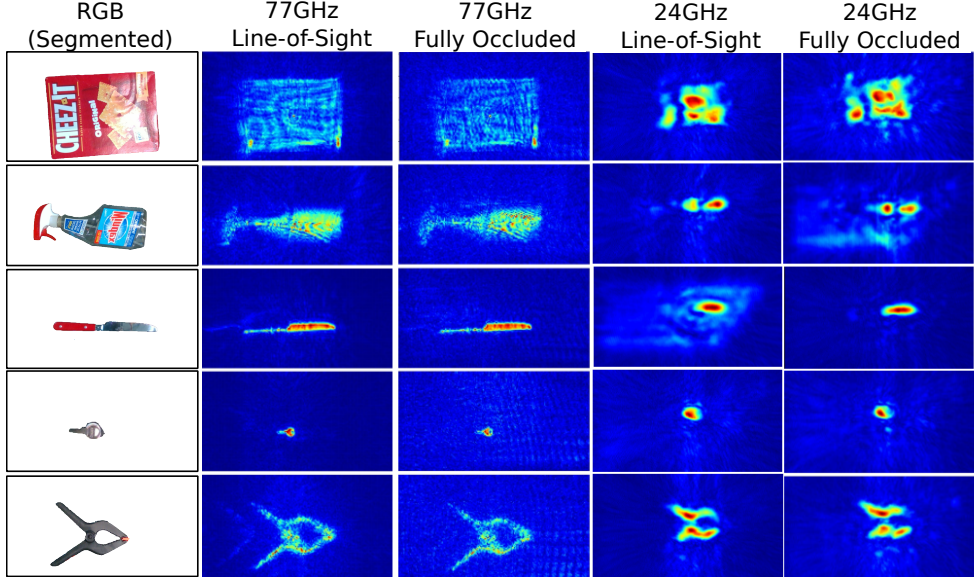


Figure 5. **Sample Images.** A number of example mmWave images within MITO.

ject datasets (e.g., YCB[17]), taken from online repositories of meshes (e.g., 3D warehouse[1] or TurboSquid[10], with millions of mesh files), or custom-generated on smartphones (e.g., PolyCam iPhone App[6]).

In addition to the mesh of the object, our simulation also takes as input the radar’s locations to simulate measurements from. At a high level, our simulation tool works by estimating the raw signals expected at each of these locations, given reflections off the target object. Then, synthetic images are produced by feeding these simulated signals into the same image processing pipeline used for real world data (Eq. 1).

Estimating the raw signal at a given location follows three steps:

1. First, we find which mesh vertices in the mesh are visible from that location [5].
2. Next, for a given visible vertex, we measure the distance to the measurement location. Given the distance, we simulate the reflection from this vertex:

$$s_j(l, v) = e^{-j \frac{4\pi |l-v|}{\lambda_j}} \quad (4)$$

where  $s_j(l, v)$  is the  $j^{\text{th}}$  sample of the reflection from location  $l$  to vertex  $v$ .

3. Finally, we sum the simulated reflections from all visible vertices to produce the raw signal for this measurement location. Formally:

$$S_j = \sum_{v \in V} s_j(l, v) \quad (5)$$

where  $S_j$  is the  $j^{\text{th}}$  sample of the simulated signal from measurement location  $l$ ,  $V$  is the set of visible vertices.

After repeating this for each measurement location, we feed the raw signals through our imaging processing pipeline to produce the final synthetic image.

Recall from Sec. 2.3 that the object’s material and texture may result in different types of reflections. To accu-

rately model different objects, we introduce 2 variations of the simulation to account for different types of reflections.

### 5.1.1 Specular Reflections.

When an object exhibits purely specular reflections, then signal will reflect off each vertex in only one direction. In some cases, the signal is reflected away from the radar’s receivers, and therefore this signal should not be added to  $S_j$ . Specifically, the signal will only be reflected back towards the radar if the surface normal is pointing directly towards the radar’s location. In any other case, the signal will be reflected away from the receiver.

We update our above simulation to account for this by removing reflections where the angle between the normal ( $\mathbf{n}$ ) and the vector from the radar to the vertex ( $l - v$ ) is less than a threshold  $\tau$ . Formally, we can update Eq. 4 to:

$$s_j(l, v) = \begin{cases} 0 & \cos^{-1}\left(\frac{\mathbf{n} \cdot (l-v)}{\|\mathbf{n}\| \|l-v\|}\right) \geq \tau \\ e^{-j \frac{4\pi |l-v|}{\lambda_j}} & \cos^{-1}\left(\frac{\mathbf{n} \cdot (l-v)}{\|\mathbf{n}\| \|l-v\|}\right) < \tau \end{cases} \quad (6)$$

Fig. 6b shows an example when simulating entirely based on specular reflections.

### 5.1.2 Edge Reflections.

In other cases, the signal experiences scattering effects from the edges of objects.<sup>7</sup> First, we define a vertex as being on an edge of an object when the angle between two of its faces is greater than an angle  $\tau_e$ , and we find the set of all vertices that lie on an edge,  $V_e$ .

Then, we replace Eq. 4 such that it only allows reflections from edge vertices.

$$s_j(l, v) = \begin{cases} 0 & v \notin V_e \\ e^{-j \frac{4\pi |l-v|}{\lambda_j}} & v \in V_e \end{cases} \quad (7)$$

Fig. 6c shows an example when simulating only reflections

<sup>7</sup>While there are more complex theories for how an RF signal reflects off edges[3], they are more computationally expensive to simulate, so we make the assumption that edges scatter uniformly.

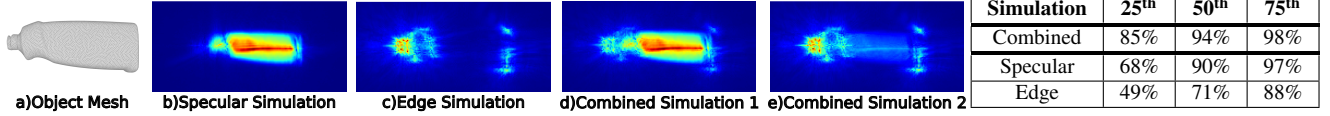


Figure 6. **Simulation Output.** Our simulation takes an a) object mesh as input and produces two different outputs assuming different reflection types: b) specular reflections and c) edge scattering. d/e) We then combine these outputs with different weights to simulate different materials.

from edges.

### 5.1.3 Combing Reflections.

In practice, materials rarely exhibit only one type of reflection, but instead some combination of the three. To account for this, our synthetic images can be added together with different weights to simulate different materials:

$$I_{syn}(\alpha_1, \alpha_2) = \frac{\alpha_1}{\alpha_1 + \alpha_2} I_s + \frac{\alpha_2}{\alpha_1 + \alpha_2} I_e \quad (8)$$

where  $I_{syn}(\alpha_1, \alpha_2)$  is the combined synthetic image for weights  $\alpha_1, \alpha_2$ , and  $I_s$  and  $I_e$  are the images from the specular, and edge simulation, respectively. Fig. 6d/e shows two examples of combining simulations with different weights representing two different materials.

## 5.2. Simulation Accuracy

To evaluate the accuracy of our simulation tool, we use the standard 3D F-Score metric [45] to compare the real-world and simulation point clouds.

### 5.2.1 Aligning the Point Clouds

Before we compute the 3D F-Score, we first need to convert both the real-world and simulation images to a point cloud. To do so, we take the 3D images, and create one point in the center of each voxel which has a power above a certain threshold  $\tau_P$ . Formally:

$$P_R = \{p \mid |I(p)| > \tau_P\} \quad P_S = \{p \mid |I_{syn}(p)| > \tau_P\}$$

where  $P_R$  and  $P_S$  are the set of points created for the real and synthetic mmWave images, respectively.

Next, we align the real-world and simulation point clouds using a standard ICP implementation[4]. This is necessary because our mmWave simulation places the object in the center of the image, while our real world experiments may have objects offset from the center.

### 5.2.2 3D F-Score

We evaluate the point cloud similarity using a standard metric, 3D F-Score[45], defined as:

$$PR = \frac{1}{N_R} \sum_{i=1}^{N_R} \mathbb{1}_{d(P_R(i), P_S) < \tau_F} \quad (9)$$

$$RE = \frac{1}{N_S} \sum_{j=1}^{N_S} \mathbb{1}_{d(P_S(j), P_R) < \tau_F}, \quad F = \frac{2 PR RE}{PR + RE} \quad (10)$$

where  $PR$ ,  $RE$ , and  $F$  are the precision, recall, and F-Score, respectively, and  $\mathbb{1}$  is an indicator variable.  $N_R$  ( $N_S$ ) is the number of points in the real (synthetic) point cloud.  $d(x, P)$  is the distance between point  $x$  and its nearest neighbor in point cloud  $P$ :  $d(x, P) = \min_{x' \in P} \|x - x'\|$ .  $\tau_F$  is the F-Score distance threshold.

Since our goal is not to select a single set of weights for each object, we compute this metric across a range of weights  $\{\alpha_1, \alpha_2\}$  and choose the combined simulation which produces the best F-Score (e.g., the simulation which best matches the properties of this real-world object).

$$F = \max_{(\alpha_1, \alpha_2) \in W} F(I_{syn}(\alpha_1, \alpha_2), I) \quad (11)$$

where  $F(I_{syn}, I)$  is the F-Score for a synthetic image  $I_{syn}$  and real-world image  $I$ .  $W$  is the set of all weights.

### 5.2.3 Results

We use the above process to compute the 3D F-Score for all objects in the dataset. We also compare to the accuracy when using only specular simulation images (i.e.,  $\alpha_1 = 1, \alpha_2 = 0$ ), and when using only edge simulation images (i.e.,  $\alpha_1 = 0, \alpha_2 = 1$ ).

Table 1 reports the 25<sup>th</sup>, 50<sup>th</sup>, and 75<sup>th</sup> percentile F-Scores for MITO (1st row), specular only (2nd row) and edge only (3rd row). MITO’s simulator achieves a median F-Score of 94%, while the specular-only or edge-only simulators achieve median F-Scores of 90% and 71%, respectively. This demonstrates the value of MITO’s techniques for combining multiple simulation types.

## 6. Using MITO for Computer Vision Tasks

### 6.1. Task 1: Object Segmentation

Here, we show how MITO can be used to build an mmWave object segmentation tool that works in LOS and NLOS.

We build on the state-of-the-art segment-anything model[28]. This model takes as input an image to segment and a prompt, either in the form of points in the image or a bounding box. The model then returns one or multiple segmentation masks, and a score associated with the predicted quality of the mask.

Using an off-the-shelf object segmentation network for mmWave images faces two challenges. First, SAM is trained on 2D RGB images, but mmWave images are single-channel, complex-valued, and 3D, and therefore cannot be used in the SAM model directly. Second, the SAM model requires a prompt before returning segmentation masks.<sup>8</sup>

Here, we describe how we address these challenges at a high-level and provide additional details in the supplementary. First, we convert our 77 GHz mmWave images to 2D RGB images start by averaging the magnitudes along the depth of the 3D image then use the rainbow colormap for

<sup>8</sup>While there are fully automatic methods using SAM, such as iterating through a grid of points as a prompt, they aim to provide all the masks within an image, and would not be sufficient in our case since they do not identify which mask contain the object of interest.



Figure 7. **mmWave Segmentation.** To segment mmWave images, we a) reduce a 2D colorized image, b) select prompt points via a mmWave power-based prompter, and c) use SAM to produce high-quality masks

colorization as shown in Fig. 7a. Second, we randomly select a subset of the highest power reflection points as prompts, as shown in Fig. 7b. By feeding the resulting RGB image and prompts to the SAM network, we can obtain mmWave segmentation as shown in the example of Fig. 7c.

**Qualitative Results.** Interestingly, in some cases, the depth camera is unable to measure the depth to every point on the object. This is typically the case for very reflective objects (e.g., mirror-like metallic objects) or clear objects (e.g., glass or plastic). In these cases, MITO is able to reconstruct more of the object than the depth camera. We show a qualitative example of this in Fig. 9. In Fig. 9b, the image from the depth camera has holes due to the object’s material reflectivity. In Fig. 9c, MITO’s mmWave image captures the whole object. Finally, Fig. 9d shows our mmWave segmentation is able to segment the entire object.

**Quantitative Results.** We evaluate the precision and recall of our segmentation across all objects. Fig. 8 plots the median precision (blue) and recall (red), with error bars denoting the 25<sup>th</sup>/75<sup>th</sup> percentiles. The figure shows a high median precision of 92.6%, which indicates that the network is not over-estimating the size of the object. Interestingly, the median recall is lower, at 64%; this is primarily because mmWave reflections are specular, as described earlier. The supplementary provides more details and §8 highlights how future work can improve recall via shape completion.

Fig. 8 additionally shows the precision and recall in the case of line-of-sight objects compared to fully occluded objects. We note that the 25<sup>th</sup>, 50<sup>th</sup>, and 75<sup>th</sup> percentile precisions vary by 2.6%, 2.3%, and 0.03%, respectively, when an object goes from LOS to fully occluded. This shows that MITO is able to accurately image and perceive fully occluded objects with a similar performance as in LOS.

## 6.2. Task 2: Object Classification (Sim2Real)

Next, we show how MITO can be used to build an object classifier. We design a classifier which takes 77GHz mmWave images as input (after applying the segmentation mask from Sec. 6.1), and outputs the estimated class label. We train the classifier entirely on synthetic data, and evaluate it on real-world images in both LOS and NLOS.

One challenge in training from synthetic images is to determine which types of reflections dominate for a given object. Recall from Sec. 5 that our simulation models two different reflection types. However, it is difficult to accurately measure the material/texture properties of all objects to identify how to correctly combine these simulation

images. Instead, we introduce a new data augmentation, whereby we randomly choose different weights for each simulation type and sum the weighted images. This allows the network to train on different material properties for each object. We also incorporate standard image augmentations (rotations, translations, erasing, blur). Additional implementation & evaluation details are in the supplementary.

**Results.** To evaluate the mmWave object classification, we trained the classifier entirely on synthetic images, and tested it on real-world measurements. Table 2 reports the results. Our classifier performs with 85% accuracy. Furthermore, it achieves an accuracy of 89% and 81% for line-of-sight and fully-occluded objects, respectively. This shows that MITO can be used for end applications such as object classification, and we expect this accuracy will improve significantly in future work.

Furthermore, we perform a microbenchmark to evaluate the impact of our different simulation types on the classifier accuracy. We retrain the classifier using only the specular simulation images (without combining them with the edge images). We repeat this process with only the edge images. Table 2 reports the accuracy of these two partial implementations in rows 4 and 5 for the specular and edge images, respectively. We note that these implementations are only able to achieve 76% and 68% each, while using both simulation types together achieved 85% accuracy. This shows the benefit of our new data augmentation leveraging our different simulation types.

These results shows that MITO has the potential to be used for NLOS applications such as confirming packaged orders in closed boxes. Further, by training on synthetic images and evaluating on real-world data, we demonstrate that the simulation is representative of the real-world.

## 7. Related Work

**Related mmWave Datasets.** Recognizing the importance of millimeter-wave perception, past research has made initial steps towards millimeter-wave datasets. However, the vast majority of them are focused either on imaging humans [18, 19, 19, 39, 48, 50] for action recognition, outdoor imaging for autonomous driving [14, 16, 23, 24, 29, 36, 37, 47, 51, 53], or imaging of building interiors (walls, hallways)[15, 38]. In the context of higher resolution imaging of objects, the only dataset that we are aware of is focused on guns and knives for TSA and detecting concealed weapons through body scanners for airport security applications [32, 40, 41]. Our work, however, is focused on generating a dataset of a larger set of generic everyday objects for application such as robotic manipulation and perception.

**mmWave Image Simulators.** Given the growth in millimeter wave devices for networking and sensing, the vast majority of existing millimeter wave simulations have also focused on understanding channel characteristics (e.g., for

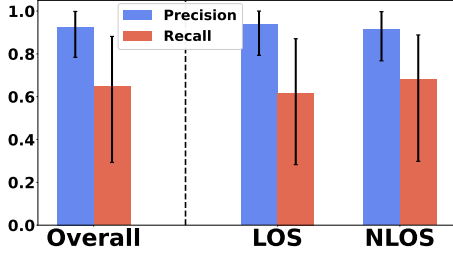


Figure 8. **mmWave Segmentation Performance.** The precision and recall for all objects, line-of-sight objects, and fully occluded items.

5G networks) [12, 34, 43] or for imaging humans for action recognition and HCI applications [49, 52, 54]. In principle, these simulators could be used also for generating datasets of everyday objects; however, existing simulators are extremely expensive, costing tens of thousands of dollars [12] and/or are limited to simulating metallic items and cannot simulate everyday objects with different properties [40]. In contrast, we developed an open-source simulation tool and demonstrated that it generates synthetic data that matches real-world collected data. We believe that this tool combined with advances in vision algorithms can lead to very high accuracy in non line of sight scenarios.

**mmWave Perception.** Past work has demonstrated the possibility of various computational tasks using millimeter waves such as autonomous vehicle & pedestrian detection [25, 30], concealed weapon detection [41, 42], car completion for autonomous driving [22, 44], or classification of entirely metallic objects [31]. Our work is inspired by the capabilities that have been demonstrated in these systems and aims to open them to a much broader community and new applications through both a dataset & simulation.

## 8. Discussions, Limitations, & Future Work

### 8.1. Non-Line-of-Sight Perception Tasks

MITO paves the way for future work in multiple directions: *mmWave Object Segmentation & Classification.* While we presented initial approaches for mmWave segmentation and classification, future work can improve these models to achieve higher accuracy. This will enable many new applications such as confirming customer orders are properly packaged in e-commerce warehouses, detecting broken objects during shipping, and other applications.

*Object Completion.* In some cases, the mmWave images do not capture the entire object (See supplementary for more details). This may be due to object specularities, where signals are reflected away from the radar, and therefore parts of the object will not be imaged. It would be interesting future work to create an object completion network that learns the missing parts of an object & creates more photo-realistic NLOS images.

*6DoF Estimation.* Another interesting problem is 6DoF estimation from mmWave images. This could be used to en-

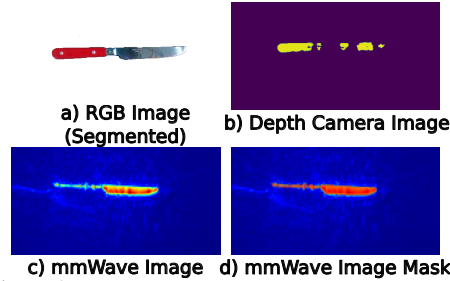


Figure 9. **Qualitative Segmentation Result.** An example where the depth image is unable to capture the entire object, but the mmWave image does.

Scenario	Accuracy
Overall	85%
Line-of-Sight	89%
Fully Occluded	81%
Specular-Only Simulation	76%
Edge-Only Simulation	68%

Table 2. **Classifier Accuracy.** Accuracy for overall, LOS, NLOS, using only specular, and only edge simulation.

sure proper liquid packaging to avoid spills, enable efficient grasp planning in NLOS (e.g., grasping an item under cloth or from within a box filled with packing peanuts), etc.

*Robotic Manipulation.* Future work can leverage many of the above NLOS perception tasks to enable new tasks in robotic manipulation. For example, accurate mmWave object segmentation and classification can significantly increase the efficiency of mechanical search and retrieval (i.e., the problem of searching for a specific item in clutter). Further, mmWave images can be used to analyze pile stability to improve push and grasp planners. NLOS perception can also help autonomous robots determine which packages contain fragile materials to be handled with special care. More generally, NLOS perception can help autonomous robots to operate in more realistic, cluttered environments.

### 8.2. Dataset Extensions.

We will continue to extend MITO’s dataset and simulation in various ways, including: (1) scenarios with multiple items, (2) other surfaces (e.g., tables) on which the items are placed, (3) additional synthetic data, e.g., 3D meshes from existing datasets in addition to real-world images here, (4) capturing objects from more angles. In addition, it would be helpful to advance the efficiency of data capture in the real-world experiments, and to speed-up our simulator.<sup>9</sup>

## 9. Conclusion

We presented MITO, the first multi-spectral mmWave dataset for everyday objects in both line-of-sight and fully-occluded settings. We provide over 580 real world images from 76 (out of 80) objects in the YCB dataset, as well as an open-source simulation tool that can be used to generate synthetic images for any 3D mesh. We showed two applications of MITO: object segmentation and classification. As we expand MITO with real and synthetic images, we hope that it enables the broader community to create the same advancements in mmWave non-line-of-sight perception that other datasets enabled for RGB perception.

<sup>9</sup>Our simulator currently takes a median of 2360 seconds to produce all synthetic signals for an object (Eqs. 4/5) and 21 seconds to produce an image (Eq. 1) when run on a computer with a Intel Core i9-10900X CPU and one GeForce RTX 2080 Ti GPU.

## References

- [1] 3d warehouse. <https://3dwarehouse.sketchup.com/>. 2, 5
- [2] Ti dca1000evm. <https://www.ti.com/tool/DCA1000EVM>. 4
- [3] Classical and modern diffraction theory. <https://library.seg.org/doi/pdf/10.1190/1.9781560803232.fm.5>
- [4] Icp registration. [https://www.open3d.org/docs/release/tutorial/pipelines/icp\\_registration.html](https://www.open3d.org/docs/release/tutorial/pipelines/icp_registration.html). 6
- [5] Perceiving systems mesh package. <https://ps.is.mpg.de/code/mesh-library>. 5
- [6] Polycam. <https://apps.apple.com/us/app/polycam-3d-scanner-lidar-360/id1532482376>. 5
- [7] Infineon position2go. <https://www.infineon.com/cms/en/product/evaluation-boards/demo-position2go/>. 4
- [8] Understanding mmwave for 5g networks. <https://www.5gamericas.org/wp-content/uploads/2020/12/InDesign-Understanding-mmWave-for-5G-Networks.pdf>. 3
- [9] Ti iwr1443boost. <https://www.ti.com/product/IWR1443#tech-docs>. 1, 4
- [10] Turbosquid. <https://www.turbosquid.com/>. 2, 5
- [11] mmWave Radar Radome Design Guide. <https://www.ti.com/lit/an/swra705/swra705.pdf>, 2021. Texas Instruments. 4
- [12] Ansys high frequency structure simulator (hfss), 2022. Ansys HFSS. 8
- [13] Fadel Adib, Chen-Yu Hsu, Hongzi Mao, Dina Katabi, and Frédo Durand. Capturing the human figure through a wall. *ACM Transactions on Graphics (TOG)*, 34(6):219, 2015. 4
- [14] Mario Bijelic, Tobias Gruber, Fahim Mannan, Florian Kraus, Werner Ritter, Klaus Dietmayer, and Felix Heide. Seeing through fog without seeing fog: Deep multimodal sensor fusion in unseen adverse weather. In *The IEEE Conference on Computer Vision and Pattern Recognition (CVPR)*, 2020. 7
- [15] Walter Brescia, Pedro Gomes, Laura Toni, Saverio Mascolo, and Luca De Cicco. Millinoise: a millimeter-wave radar sparse point cloud dataset in indoor scenarios. In *Proceedings of the 15th ACM Multimedia Systems Conference*, pages 422–428, 2024. 7
- [16] H. Caesar, V. Bankiti, A. H. Lang, S. Vora, V. Liong, Q. Xu, A. Krishnan, Y. Pan, G. Baldan, and O. Beijbom. nuscenes: A multimodal dataset for autonomous driving. In *2020 IEEE/CVF Conference on Computer Vision and Pattern Recognition (CVPR)*, pages 11618–11628, Los Alamitos, CA, USA, 2020. IEEE Computer Society. 7
- [17] Berk Calli, Arjun Singh, James Bruce, Aaron Walsman, Kurt Konolige, Siddhartha Srinivasa, Pieter Abbeel, and Aaron M Dollar. Yale-cmu-berkeley dataset for robotic manipulation research. *The International Journal of Robotics Research*, 36(3):261–268, 2017. 2, 3, 5
- [18] Anjun Chen, Xiangyu Wang, Shaohao Zhu, Yanxu Li, Jiming Chen, and Qi Ye. mmbody benchmark: 3d body reconstruction dataset and analysis for millimeter wave radar, 2022. 7
- [19] Han Cui, Shu Zhong, Jiacheng Wu, Zichao Shen, Naim Dahoun, and Yiren Zhao. Milipoint: A point cloud dataset for mmwave radar, 2023. 7
- [20] M. Everingham, L. Van Gool, C. K. I. Williams, J. Winn, and A. Zisserman. The pascal visual object classes (voc) challenge. *International Journal of Computer Vision*, 88(2): 303–338, 2010. 2
- [21] Simon Fothergill, Helena Mentis, Pushmeet Kohli, and Sebastian Nowozin. Instructing people for training gestural interactive systems. In *Proceedings of the SIGCHI Conference on Human Factors in Computing Systems*, page 1737–1746, New York, NY, USA, 2012. Association for Computing Machinery. 2
- [22] Junfeng Guan, Sohrab Madani, Suraj Jog, Saurabh Gupta, and Haitham Hassanieh. Through fog high-resolution imaging using millimeter wave radar. In *IEEE/CVF Conference on Computer Vision and Pattern Recognition (CVPR)*, 2020. 8
- [23] Junfeng Guan, Sohrab Madani, Suraj Jog, Saurabh Gupta, and Haitham Hassanieh. Through fog high-resolution imaging using millimeter wave radar. In *Proceedings of the IEEE/CVF Conference on Computer Vision and Pattern Recognition (CVPR)*, 2020. 7
- [24] Runwei Guan, Ruixiao Zhang, Ningwei Ouyang, Jianan Liu, Ka Lok Man, Xiaohao Cai, Ming Xu, Jeremy Smith, Eng Gee Lim, Yutao Yue, et al. Talk2radar: Bridging natural language with 4d mmwave radar for 3d referring expression comprehension. *arXiv preprint arXiv:2405.12821*, 2024. 7
- [25] Siddharth Gupta, Prabhat Kumar Rai, Abhinav Kumar, Phaneendra K. Yalavarthy, and Linga Reddy Cenkeramaddi. Target classification by mmwave fmcw radars using machine learning on range-angle images. *IEEE Sensors Journal*, 21(18):19993–20001, 2021. 8
- [26] Intel RealSense. <https://www.intelrealsense.com>, 2019. 4
- [27] Allison Janoch, Sergey Karayev, Yangqing Jia, Jonathan T. Barron, Mario Fritz, Kate Saenko, and Trevor Darrell. A category-level 3-d object dataset: Putting the kinect to work. In *2011 IEEE International Conference on Computer Vision Workshops (ICCV Workshops)*, pages 1168–1174, 2011. 2
- [28] Alexander Kirillov, Eric Mintun, Nikhila Ravi, Hanzi Mao, Chloe Rolland, Laura Gustafson, Tete Xiao, Spencer Whitehead, Alexander C. Berg, Wan-Yen Lo, Piotr Dollár, and Ross Girshick. Segment anything. *arXiv:2304.02643*, 2023. 2, 6
- [29] Andrew Kramer, Kyle Harlow, Christopher Williams, and Christoffer Heckman. Coloradar: The direct 3d millimeter wave radar dataset. *The International Journal of Robotics Research*, 41(4):351–360, 2022. 7
- [30] Mohamed Lamane, Mohamed Tabaa, and Abdessamad Klilou. Classification of targets detected by mmwave radar using yolov5. *Procedia Computer Science*, 203:426–431, 2022. 17th International Conference on Future Networks

- and Communications / 19th International Conference on Mobile Systems and Pervasive Computing / 12th International Conference on Sustainable Energy Information Technology (FNC/MobiSPC/SEIT 2022), August 9-11, 2022, Niagara Falls, Ontario, Canada. 8
- [31] Jie Liu, Kai Zhang, Zhenlin Sun, Qiang Wu, Wei He, and Hao Wang. Concealed object detection and recognition system based on millimeter wave fmcw radar. *Applied Sciences*, 11(19), 2021. 8
- [32] Ting Liu, Yao Zhao, Yunchao Wei, Yufeng Zhao, and Shikui Wei. Concealed object detection for activate millimeter wave image. *IEEE Transactions on Industrial Electronics*, 66(12): 9909–9917, 2019. 7
- [33] Jonathan S. Lu, Patrick Cabrol, Daniel Steinbach, and Ravikummar V. Pragada. Measurement and characterization of various outdoor 60 ghz diffracted and scattered paths. In *MILCOM 2013 - 2013 IEEE Military Communications Conference*, pages 1238–1243, 2013. 3
- [34] Marco Mezzavilla, Menglei Zhang, Michele Polese, Russell Ford, Sourjya Dutta, Sundeeep Rangan, and Michele Zorzi. End-to-end simulation of 5g mmwave networks. *IEEE Communications Surveys & Tutorials*, 20(3):2237–2263, 2018. 8
- [35] Jeffrey A Nanzer. *Microwave and millimeter-wave remote sensing for security applications*. Artech House, 2012. 2
- [36] Dong-Hee Paek, Seung-Hyun Kong, and Kevin Tirta Wijaya. K-radar: 4d radar object detection for autonomous driving in various weather conditions. In *Thirty-sixth Conference on Neural Information Processing Systems Datasets and Benchmarks Track*, 2022. 7
- [37] Andras Palffy, Ewoud Pool, Srimannarayana Baratam, Julian F. P. Kooij, and Dariu M. Gavrilu. Multi-class road user detection with 3+1d radar in the view-of-delft dataset. *IEEE Robotics and Automation Letters*, 7(2):4961–4968, 2022. 7
- [38] Akarsh Prabhakara, Tao Jin, Arnav Das, Gantavya Bhatt, Lilly Kumari, Elahe Soltanaghahi, Jeff Bilmes, Swarun Kumar, and Anthony Rowe. Radarhd: Demonstrating lidar-like point clouds from mmwave radar. In *Proceedings of the 29th Annual International Conference on Mobile Computing and Networking*, pages 1–3, 2023. 7
- [39] M Mahbubur Rahman, Ryoma Yataka, Sorachi Kato, Pu Perry Wang, Peizhao Li, Adriano Cardace, and Petros Boufounos. Mmvr: Millimeter-wave multi-view radar dataset and benchmark for indoor perception. *arXiv preprint arXiv:2406.10708*, 2024. 7
- [40] Hem Regmi, Moh Sabbir Saadat, Sanjib Sur, and Srihari Nelakuditi. Squigglemilli: Approximating sar imaging on mobile millimeter-wave devices. *Proc. ACM Interact. Mob. Wearable Ubiquitous Technol.*, 5(3), 2021. 7, 8
- [41] Bofeng Su and Minghui Yuan. Object recognition for millimeter wave mimo-sar images based on high-resolution feature recursive alignment fusion network. *IEEE Sensors Journal*, 23(14):16413–16427, 2023. 7, 8
- [42] Peng Sun, Ting Liu, Xiaotong Chen, Shiyin Zhang, Yao Zhao, and Shikui Wei. Multi-source aggregation transformer for concealed object detection in millimeter-wave images. *IEEE Transactions on Circuits and Systems for Video Technology*, 32(9):6148–6159, 2022. 8
- [43] Shu Sun, George R MacCartney, and Theodore S Rappaport. A novel millimeter-wave channel simulator and applications for 5g wireless communications. In *2017 IEEE international conference on communications (ICC)*, pages 1–7. IEEE, 2017. 8
- [44] Y. Sun, Z. Huang, H. Zhang, Z. Cao, and D. Xu. 3drimr: 3d reconstruction and imaging via mmwave radar based on deep learning. In *2021 IEEE International Performance, Computing, and Communications Conference (IPCCC)*, pages 1–8, Los Alamitos, CA, USA, 2021. IEEE Computer Society. 8
- [45] Maxim Tatarchenko\*, Stephan R. Richter\*, René Ranftl, Zhuwen Li, Vladlen Koltun, and Thomas Brox. What do single-view 3d reconstruction networks learn? 2019. 6
- [46] Universal Robots, UR5e. <https://www.universal-robots.com/products/ur5-robot/>, 2021. 4
- [47] Yizhou Wang, Jen-Hao Cheng, Jui-Te Huang, Sheng-Yao Kuan, Qiqian Fu, Chiming Ni, Shengyu Hao, Gaoang Wang, Guanbin Xing, Hui Liu, et al. Vision meets mmwave radar: 3d object perception benchmark for autonomous driving. In *2024 IEEE Intelligent Vehicles Symposium (IV)*, pages 2769–2775. IEEE, 2024. 7
- [48] Zhongce Wang, Chao Jin, Lingzhang Sun, and Yunfan Li. Wrdi: A multimodal dataset of mmwave radar data and image. In *2021 IEEE International Conference on Big Data (Big Data)*, pages 3209–3214, 2021. 7
- [49] Sahil Waqar and Matthias Pätzold. A simulation-based framework for the design of human activity recognition systems using radar sensors. *IEEE Internet of Things Journal*, 2023. 8
- [50] Yingxiao Wu, Zhongmin Jiang, Haocheng Ni, Changlin Mao, Zhiyuan Zhou, Wenxiang Wang, and Jianping Han. mmhpe: Robust multi-scale 3d human pose estimation using a single mmwave radar. *IEEE Internet of Things Journal*, 2024. 7
- [51] Jianjian Yang, Tianmu Gui, Yibo Tong, Yuyuan Zhang, Qiankun Huang, and Guanghui Zhao. Autonomous mining transportation systems: Integrating 4d mmwave radar for enhanced detection of obstructed static objects. *IEEE Transactions on Intelligent Vehicles*, 2024. 7
- [52] Xiaotong Zhang, Zhenjiang Li, and Jin Zhang. Synthesized millimeter-waves for human motion sensing. In *Proceedings of the 20th ACM Conference on Embedded Networked Sensor Systems*, page 377–390, New York, NY, USA, 2023. Association for Computing Machinery. 8
- [53] Lianqing Zheng, Zhixiong Ma, Xichan Zhu, Bin Tan, Sen Li, Kai Long, Weiqi Sun, Sihan Chen, Lu Zhang, Mengyue Wan, Libo Huang, and Jie Bai. Tj4dradset: A 4d radar dataset for autonomous driving. In *2022 IEEE 25th International Conference on Intelligent Transportation Systems (ITSC)*, pages 493–498, 2022. 7
- [54] Junyu Zhou and Julien Le Kernec. 4d radar simulator for human activity recognition. *IET Radar, Sonar & Navigation*, 2023. 8